Velocity Structure of the Subducting Nazca Plate beneath central Peru as inferred from Travel Time Anomalies

by

Edmundo O. Norabuena

Thesis submitted to the faculty of the

Virginia Polytechnic Institute and State University

in partial fulfillment of the requirements for the degree of

MASTER OF SCIENCE

in

Geophysics

APPROVED:

J. Arthur Snoke, Chairman

G. A. Bollinger   D. E. James

December, 1992

Blacksburg, Virginia

Velocity Structure of the Subducting Nazca Plate beneath central Peru as inferred from Travel Time Anomalies

by

Edmundo O. Norabuena

Committee Chairman: J. Arthur Snoke

Geological Sciences

(ABSTRACT)

Arrival times from intermediate-depth (110-150 km) earthquakes within the region of flat subduction beneath central Peru provide constraints on the geometry and velocity structure of the subducting Nazca plate. Hypocenters for these events, which are beneath the sub-andean and eastern Peruvian basins, were determined using a best-fitting one-dimensional velocity-depth model with a 15-station digitally-recording network deployed in the epicentral region. For that model, P-wave travel times to coastal stations, about $6°$ trenchward, exhibit negative residuals of up to 4 seconds and have considerably more complexity than arrivals at the network stations.

The residuals at coastal stations are conjectured to result from travel paths with long segments in the colder, higher velocity subducting plate. Travel time anomalies were modeled by 3-D raytracing. Computed ray paths show that travel times to coastal stations for the eastern Peru events can be satisfactorily modeled if velocities relative to the surrounding mantle are 6% lower within the uppermost slab (a 6 km thick layer composed of basaltic oceanic crust) and 8% higher within the cold peridotitic layer (which must be at least 44 km thick). Raytracing runs for this plate model show that "shadow zones" can occur if the source-slab-receiver geometry results in seismic rays passing through regions in which the slab undergoes significant changes in slope. Such geometries exist for seismic waves propagating to some coastal stations from sources located beneath the eastern Peruvian basin. Observed first-arrival times for such cases do in fact have less negative residuals than those for geometries which allow for "direct" paths. Modeling such arrivals as trapped mode propagation through the high-velocity part of the plate produces arrival times consistent with those observed.

ACKNOWLEDGEMENTS

TABLE OF CONTENTS

CONTENTS

LIST OF FIGURES

LIST OF FIGURES

LIST OF TABLES

Chapter 1
OVERVIEW

The present study examines the high velocity propagation of longitudinal waves through the region of flat subduction beneath northern and central Peru in the central Andean region of western South America, Figure 1.1. Analysis of travel times associated with these seismic waves are used to place constraints on the geometry of the slab and its velocity structure. To carry out the analysis we selected a suite of intermediate depth events (focal depths between $110 - 155$ km) that occurred beneath eastern-central Peru, and which were well recorded by two different networks: a local array of portable digital recorders and a permanent telemetered array located along the Peruvian coast. The local network, deployed for a period of several weeks in the epicentral region, constituted the locator array, while the telemetered network was used to measure travel time anomalies for seismic waves traveling within the slab to the coast.

High quality hypocentral determination for the suite of events were obtained from the locator array based on a regional 1-D velocity structure. Calculated travel times for direct P-waves to coastal stations based on the same 1-D velocity structure were all slow with respect to the observed times. Moreover, no 1-D model was found that would produce uniformly small residuals. Residuals to the coastal stations, all negatives, were considered too large to be caused by heterogeneities beneath the station or by inaccuracy in timing or phase reading. These large negative residuals suggest the possibility that the traveltime anomalies are caused by ray propagation through the cold and hence high velocity interior of the slab. Based on existing knowledge about oceanic lithosphere, the subducting Nazca plate, Figure 1.2, is modeled as a 3-D structure composed of three layers: a thin basaltic layer, a cold interior peridotitic layer and a transitional region between cold interior and

the asthenosphere.

Modeling shows that P-wave travel times to coastal stations can be explained by rays propagating through the subducting plate whose velocities in the first two layers are respectively 6% lower and 8% higher than the surrounding mantle. In addition, 3-D raytracing shows that the slab geometry causes shadow zones (regions not illuminated by direct P-wave arrivals), and where these occur, the first arrival at coastal stations results from a wave trapped within the high velocity layer. The existence of such shadow zones provides information as to morphology of the slab surface and velocity distribution within the slab.
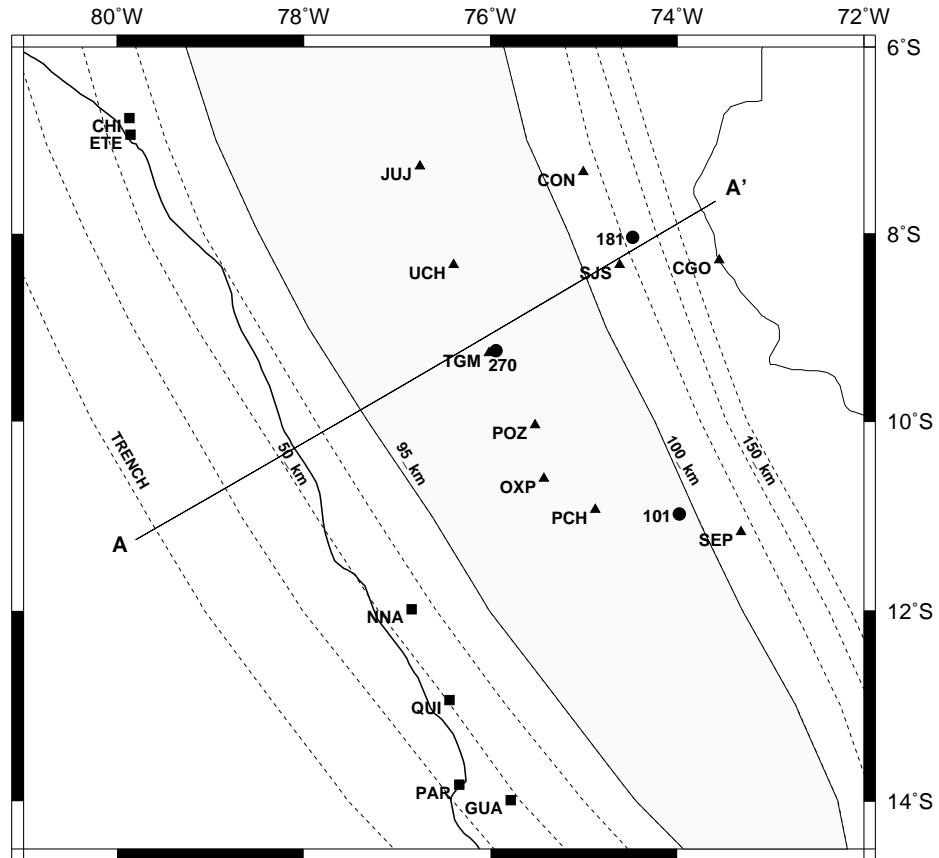
Figure 1.1: Distribution of seismic stations during the PE85 experiment. Coastal network stations are represented by solid circles and stations of the locator network by solid triangles. Epicenters for the three events under study are shown as filled circles. Dashed lines represent isodepth contours of the Nazca Plate at intervals of 25 km except the 95 and 100 km levels which delimit the region of flat subduction. Line $A - A'$ represent direction of projection for Figure 1.2
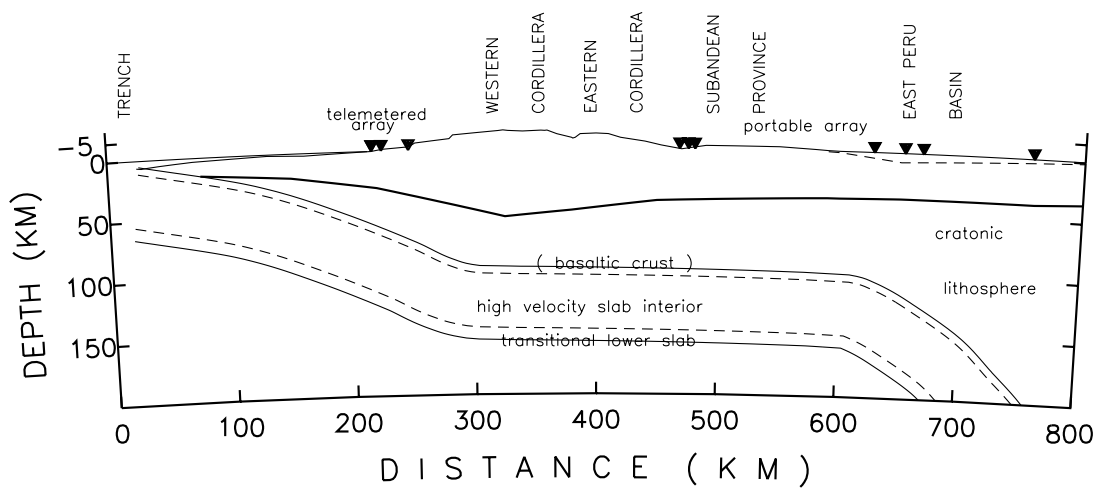
Figure 1.2: Structure of the Nazca plate subducting beneath central Peru. The model suggest a thin uncoverted basaltic crust on the top, a cold high velocity interior layer and a transitional region. The 800 km cross section has its origin at 11.25° S and 79.8° W and a 62° azimuth. The inverted solid triangles map the geometry of the seismic networks.

Chapter 2
TECTONIC SETTING

The western coast of South America is the only major active margin along which an oceanic plate (Nazca Plate) underthrusts a continent (South America). Numerous studies based on seismicity and geological data have shown that the Andean margin can be subdivided into five tectonic segments between latitudes 0°S and 45°S [e.g., Stauder, 1975; Barazangi and Isacks 1976; Jordan *et al.*, 1983]. These segments alternate between modes of normal and flat subduction. Zones of normal subduction, Figure 2.1, are associated with an active volcanic front (southern Ecuador, southern Peru and northern Chile, and southern Chile). In contrast, flat subduction zones are characterized by the absence of volcanos (northern-central Peru and central Chile). Our study focuses on the segment bounded by latitudes 5° S and 15° S , considered the largest zone of flat subduction in the world. In that region the Nazca Plate descends at about 30° dip until it reaches the approximate depth of 100 km, where it flattens and runs sub-horizontally for several hundred kilometers before dipping steeply into the upper mantle [Hasegawa and Sacks, 1981].

The existence of horizontal subduction appears to be related to the history of igneous activity in the region [e.g., Noble *et al.*, 1974; Barazangi and Isacks, 1976; Noble and McKee, 1977]. The latter study based on radiometric age analysis and interpretation of geological records, presented a plausible scenario in which the Neogene volcanism along northern and central Peru ended gradually 5 m.y. ago, early Pliocene, after a strong pulse of magmatic and volcanic activity (9.5 m.y.). This geological interpretation correlates with low terrestrial heat flow observations that average 30 mW/m^2 over the volcanic-free zones. In contrast, the values commonly measured above regions of normal subduction reach 60 mW/m^2 [Henry, 1981; Henry and Pollack, 1988]. Moreover, the crust and upper mantle exhibit low seismic

wave absorption (high Q) [Hasegawa and Sacks, 1981, 1988; Schneider and Sacks, 1991].

Following Ham and Herrera (1969), Megard (1984, 1987) and James and Snoke (1992), the region of study is divided into the following main geological provinces as shown in Figure 2.2 :

- The *Coastal zone* is a narrow band, desertic in most of its extension, underlain by the so called coastal batholith. Marine sedimentary basins of Tertiary age characterize the coastal region north of 5° S and south of 13.5° S.

- The *Western Cordillera* represents a morphological and structural asymmetry about 150 km across. Its western side consists of a dipping isoclinal fold of marine Mesozoic sediments that reach elevations of 5000 m. From 5° S to 12° S the Western cordillera parallels the Eastern cordillera. South of 12° S, the eastern slope of the Western cordillera borders the Altiplano and rises to elevations of up to 1000 m above it.

- The *Eastern Cordillera* is a fold and thrust mountain belt bordering the Western Cordillera, reaching a maximum elevation of 6000 m. Rocks strongly faulted and folded with a high degree of metamorphism are widespread throughout the region. Sedimentary Paleozoic and Mesozoic rocks overlay a Pre-cambrian basement that outcrops extensively. The overall deformation in this area is expressed by open folds and steep thrusts dipping SW.

- The *Sub-Andean belt* is the eastward migrating edge of the Andean tectonism. It comprises the foothills of the Eastern Cordillera and includes the tectonically active Andean front where it butts against the Brazilian shield. Elevations reach a maximum of 2000 m but decrease steadily toward the East. Thrust and fold belts are characteristic of this zone.

- The *Eastern Peru basin* groups are situated mainly in the highly forested Ucayali and Amazon basins. The basins are comprised of Paleozoic and Mesozoic sediments of marine nature which are overlain by massive continental deposits of Tertiary age.

The deposits have been faulted and folded most extensively at the Andean margin, but deformation decreases toward the East where the sedimentary layer thins onto the Brazilian shield.
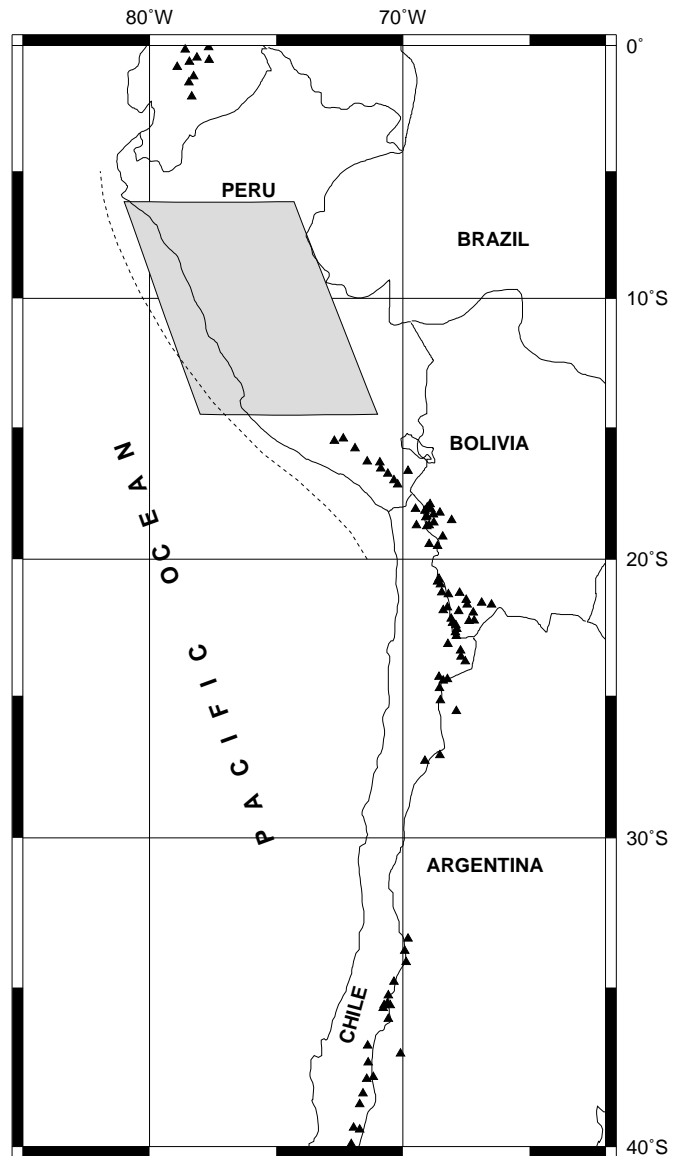
Figure 2.1: This map delineates the volcanic regions developed along the western coast of South America (solid triangles). Under the regions bounded by (0°S - 2°S), (15°S - 27°S) and (33°S - 45°S) the Nazca plate subducts at normal angles of about 30°. The regions of no-volcanos correspond to the flat subduction zones of northern-central Peru and central Chile. Shaded area marks the area of study and the Peru-Chile trench is indicated by a dashed line.
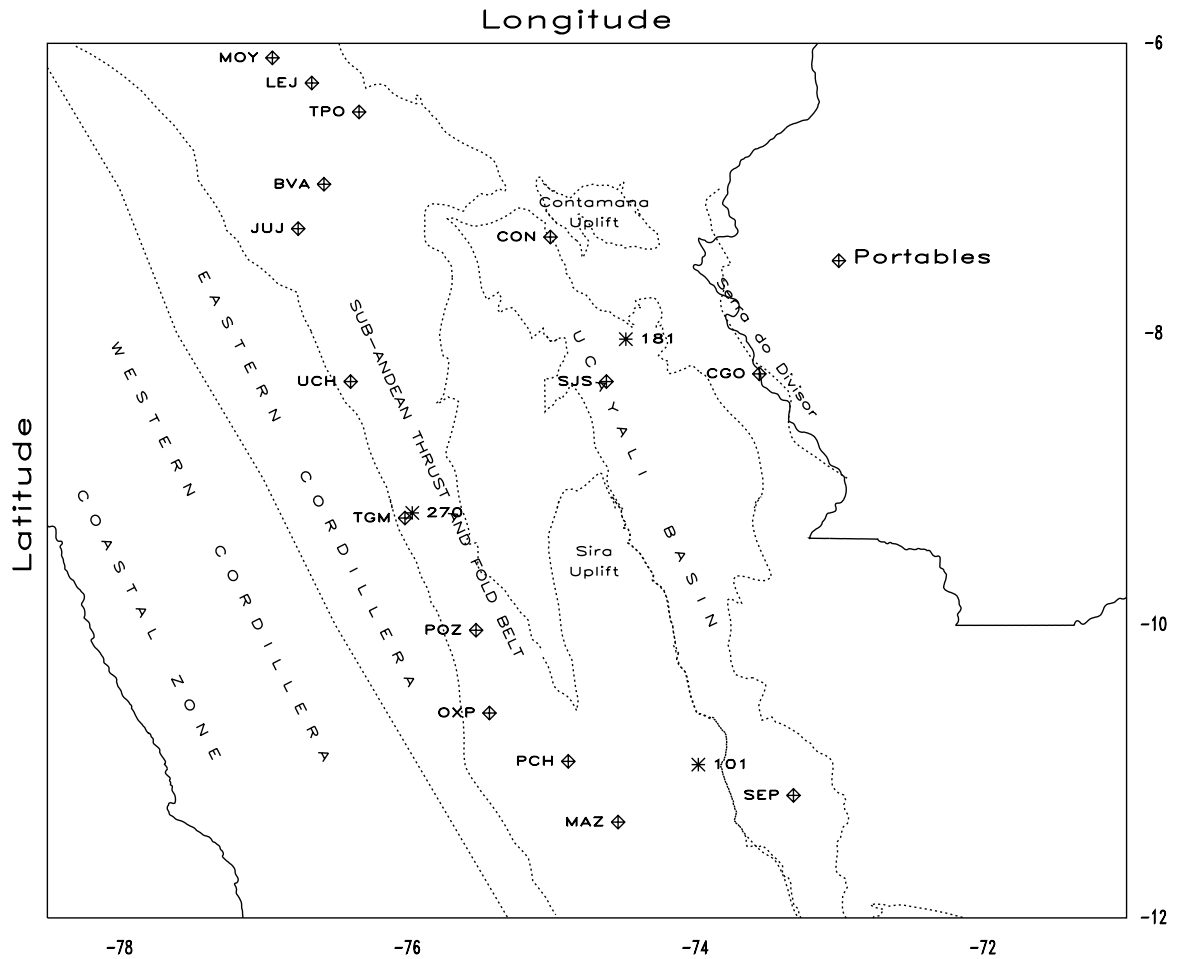
Figure 2.2: Mapview of central Peru outlining its main geological provinces. The area of study is bounded by latitudes 5°S to 15°S and longitudes 79° W to 72° W.

Chapter 3

DATA

3.1 Introduction

The events used in this study are from the data set obtained in 1985 during an experiment carried out by the Department of Terrestrial Magnetism (DTM/CIW) and the Geophysical Institute of Peru (IGP) over the Andean and Basin provinces of central-eastern Peru [Schneider and Sacks, 1991]. A vertical cross-section presenting the intermediate focal depth earthquakes located in the 1985 Peru experiment (PE85) is shown in Figure 3.1. The section has been taken in a direction perpendicular to the trench at $10.27°$ S and $78.51°$ W. The three principal events used in this study referred to henceforth as E101, E181 and E270, were well recorded by both the local network and by a regional coastal network. The particular geometry between seismic sources and coastal stations is optimum for having seismic waves to travel long distance within the slab, a fact that makes our data set unique and valuable. Figure 1.1 shows the location of the local and coastal networks, and hypocenters of events used in this study. Table 3.1 shows the geographical coordinates of the portable and coastal network stations. A description of the seismic networks is given below, followed by a description of the data processing procedures.

3.2 Seismic Networks

- **Local Network:** The local network consisted of fourteen digital seismographs composed mainly of University of Wisconsin recorders (UWR) and provided with three 1 Hz geophones in orthogonal configuration (Z, NS and EW). Figure 1.1 shows locations of these recorders as solid triangles. Kinemetrics PDR-1s and Sprenghneter

-10.274 -78.512 60.00 600.00 800.00

PERU perpendicular to trench

DISTANCE (KM)
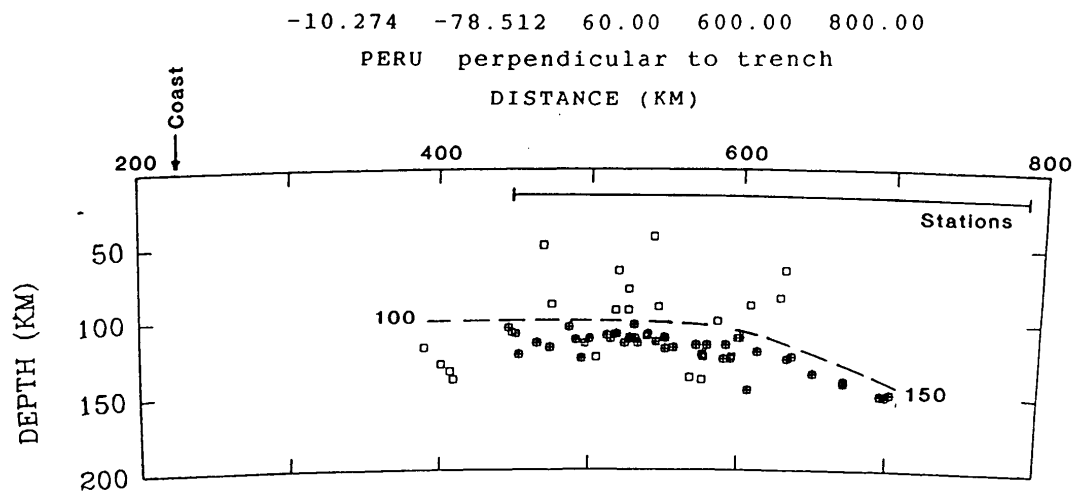
Figure 3.1: Intermediate depth earthquakes recorded beneath the central-eastern Peru region delineating the flat subduction zone. The cross-section corresponds to a 600 km segment starting from 10.27° S and 78.51° W with a 60° strike. Filled circles represent events with better constrained locations. After Schneider and Sacks, 1991.

DR100s were used in some of the stations but the analysis of data was restricted to the UWRs whose accuracy in time were better than 0.01 sec since they used Omega clock receivers. Timing for the PDR1s and DR100s relied on high precision crystals oscillators that were periodically synchronized with GOES satellite clock.

- **Coastal Network:** The coastal network consisted of five telemetered stations (CHI, ETE, QUI, PAR and GUA) provided with 1 Hz vertical geophones and one analog WWSSN station (NNA). The data from the telemetered stations were recorded digitally at a central recording site including information from a GOES satellite clock. A feature of this network, including NNA, is its alignment approximately parallel to the trench.

The local network was operational for approximately three months during which a total of 512 events were recorded. Eighty intermediate depth focus earthquakes, all of them located within the flat portion of the subducting slab, were cataloged as the PE85 data set. Although 25 of these events were also recorded by the coastal array, only events E101, E181 and E270 had hypocenters located within the local network but with clear arrivals at all the coastal stations.

3.3 Data Processing

Seismograms from the local stations and those corresponding to the telemetered network were analyzed interactively by means of the Seismic Analysis Code (SAC rev 10.6d) [Tull, 1991] running on a Sun-Sparc platform.

For the local stations, P-wave arrivals were selected from seismograms of the unfiltered vertical component while S-wave arrivals were selected from the horizontal components (NS and EW). The information of phase arrivals was then extracted from the SAC header files to generate a driver file for the locator program Hypoellipse [Lahr, 1992]. The seismograms for event E101, E181 and E270 are presented in figures 3.2, 3.3 and 3.4 respectively. The high

frequency content exhibit by these records suggest their passage through a low absorptive (high Q) propagation medium.

The complexity exhibited by the seismograms at the coastal stations, as shown from figures 3.5, 3.6 and 3.7, and the lack of horizontal components restricted phase identification to first P-wave arrivals. To eliminate high frequency noise, the seismograms were lowpass filtered with a 4-pole Butterworth filter band limited to 8 Hz. The signal to noise ratio of the telemetered records for event E181 at stations ETE and CHI were so poor that phase arrivals to these stations were obtained from the IGP seismic bulletins. Arrivals to station NNA, a WWSSN analog station, were taken from the same bulletins.

Table 3.1: Station codes and coordinates of seismic stations used by the PE85 experiment.

Station	Code	Latitude (deg)	Longitude (deg)	Elevation (meters)
Chiclayo	CHI	-06.765	-79.865	60
Eten	ETE	-06.940	-79.855	200
Nana	NNA	-11.988	-76.842	575
Quilmana	QUI	-12.943	-76.437	510
Paracas	PAR	-13.829	-76.331	220
Guadalupe	GUA	-13.992	-75.783	550
Cantagallo	CGO	-08.279	-73.552	241
Contamana	CON	-07.337	-75.004	196
Juanjui	JUJ	-07.279	-76.757	500
Mazamari	MAZ	-11.348	-74.534	750
Oxapampa	OXP	-10.604	-75.428	1850
Pichis	PCH	-10.934	-74.880	700
Pozuzo	POZ	-10.038	-75.521	960
Sepahua	SEP	-11.166	-73.315	348
San Jose	SJS	-08.332	-74.615	192
TingoMaria	TGM	-09.269	-76.015	700
Uchiza	UCH	-08.332	-76.393	540
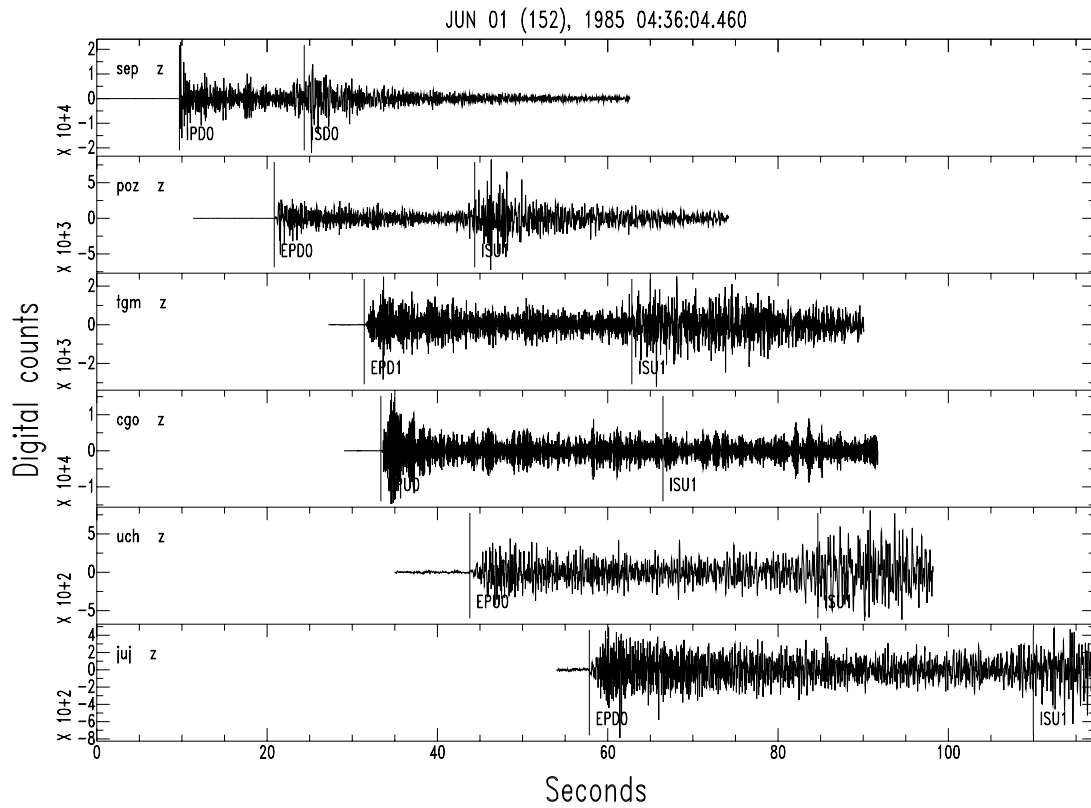
Figure 3.2: Seismograms of event E101 recorded by the local network. Traces correspond to unfiltered vertical components from 1 Hz geophones. P and S arrivals are indicated. (S arrival times were picked from horizontal records.)
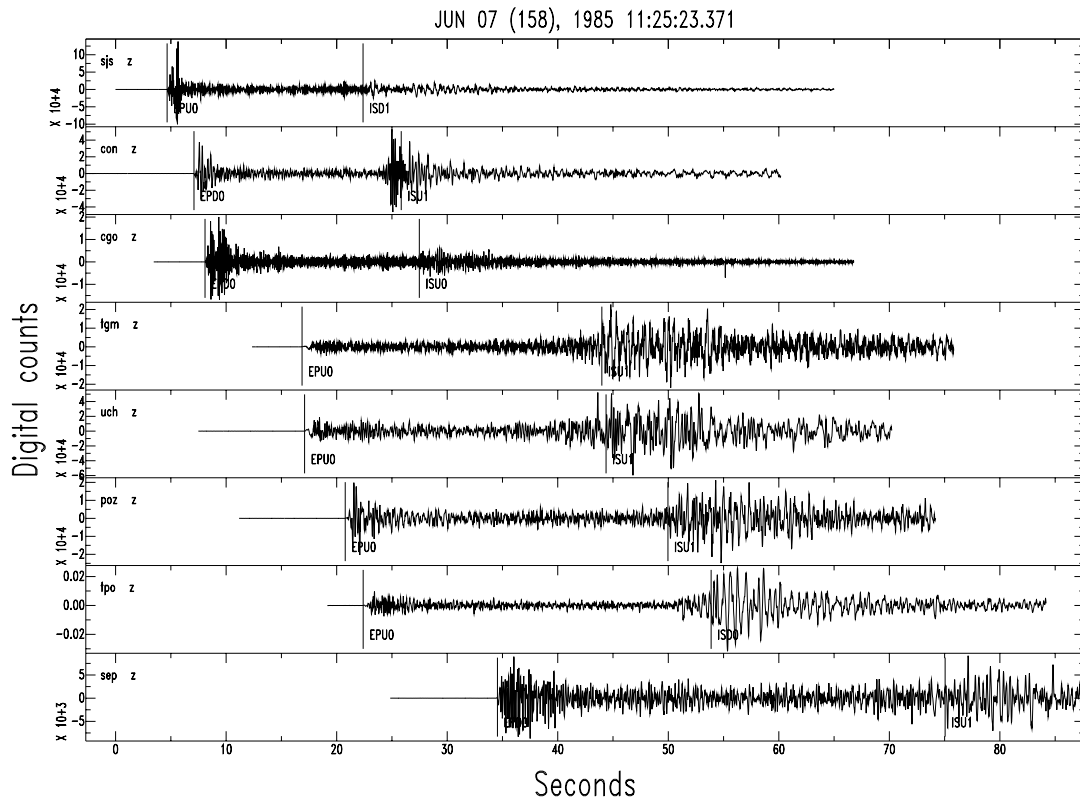
Figure 3.3: Seismograms for event E181 recorded by the local network. Traces correspond to unfiltered vertical components from 1 Hz geophones. P and S arrivals are indicated.

16
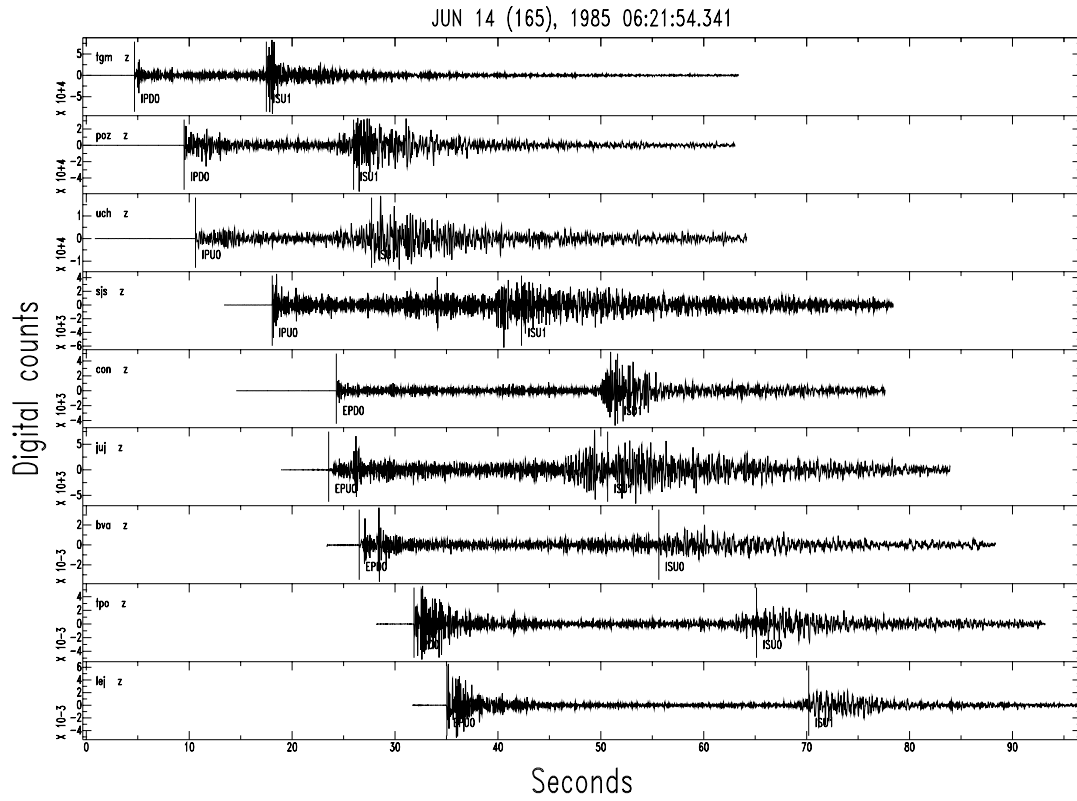
Figure 3.4: Seismograms recorded at stations of the local network for event E270. Traces correspond to unfiltered vertical components showing P and S arrivals.

17
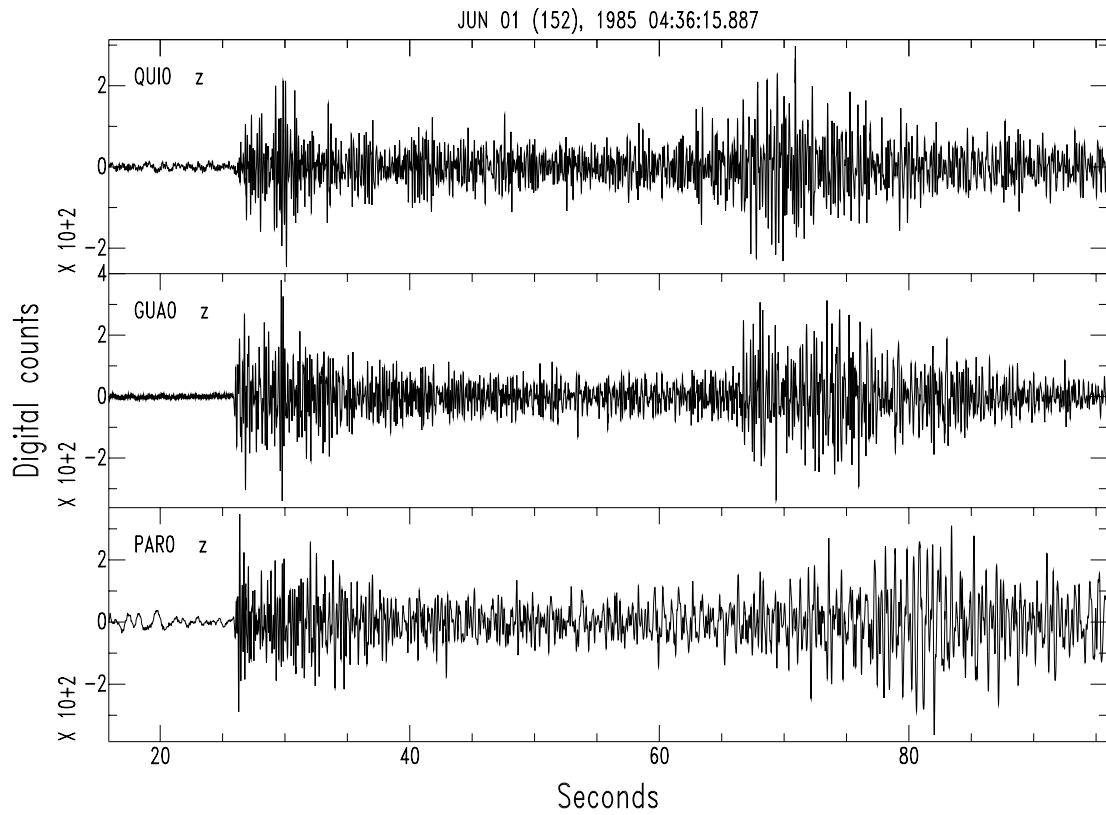
Figure 3.5: Seismograms for event E101 recorded at coastal network. Traces have been aligned with the first arrival and correspond to vertical components lowpass filtered at 8 Hz.

Figure 3.6: Seismograms for event E181 recorded at coastal network. Traces have been aligned with the first arrival and correspond to vertical components lowpass filtered at 8 Hz.

Figure 3.7: Seismograms for event E270 at coastal network. Traces have been aligned with the first arrival and correspond to vertical components lowpass filtered at 8 Hz.

Chapter 4
HYPOCENTER LOCATIONS

4.1 Introduction

Travel time residuals of compressional waves traveling regional distances to coastal stations are used to put constraints on the geometry and velocity structure of the Nazca plate segment that subducts beneath northern-central Peru. As a consequence, accuracy in hypocentral locations is a fundamental requirement for this study.

Early studies on the seismicity and, inferentially, on the geometry of the Nazca plate beneath northern-central Peru were based on teleseismic data [e.g., Barazangi and Isacks, 1976]. More recent studies by Hasegawa and Sacks (1981), Boyd *et al.*, (1984) and Schneider *et al.*, (1987), using data from a local seismic network in southern Peru, obtained well determined locations for about 2000 events that were a primary constraint on the geometry of the plate model I have used. It was not until the PE85 experiment that high quality recordings of earthquakes occurring beneath central-eastern Peru were obtained. These earthquakes, located within the flat segment of the slab and in the region close to the resubduction zone (Figure 3.1), comprise the database from which we extracted the suite of events used in the present study.

The sources of the selected events were located in the slab at depths of about 110-150 km and generated seismic rays that traveled almost vertically to the locator network stations. Consequently, sources of error common to subduction zones as reported by Engdahl *et al.*, (1982) and McLahren and Frohlich (1985) have minimal effect in the data set used in this study.

4.2   Flat Earth vs Spherical Earth

Standard locator programs such as Hypo71 [Lee and Lahr, 1971], Hypoinverse [Klein, 1978], and Fasthypo [Herman, 1979] have been the common tools for locating events at local and regional distances. All of these methods model velocity structures as horizontal layers in a flat earth. Preliminary locations for the PE85 data set were obtained using flat earth modeling. Although results obtained with these methods could be considered appropriate for shallow crustal events at distances less than 2.5^o [Peters, 1973], they must be examined critically when locating deeper events at any epicentral distance.

In examining station-event geometries such as those found in our data set, differences in travel times between flat and spherical earth models can be significant. To quantify this observation, a one-dimensional velocity-depth model was used to calculate theoretical travel times from two sources located at 100 and 150 km depth to receivers covering a distance range from 0 to 800 km ($7.2°$). Each source led to two sets of travel-times: one associated with propagation through a flat earth model (t_{flat}) and the other associated with propagation through a spherical earth model (t_{sph}). Figure 4.1 shows the travel time difference between both models ($t_{flat} - t_{sph}$) as function of epicentral distance. The resultant curves show that deviation in travel time increases systematically with epicentral distance and with depth. Errors up to 1.0 seconds can be easily attained at a distance of 600 km for hypocenters with a focal depth of 150 km if flat-earth modeling is chosen. S arrivals for the same distances and focal depths will lead to time differences larger by a factor of about 1.8.

To avoid such systematic errors, we used spherical earth modeling for our final locations. We note in passing that there are other studies which have used spherical earth modeling for calculating earthquakes at local and regional distances [e.g., Engdahl, 1973; Engdahl *et al.*, 1976; Engdahl *et al.*, 1982].
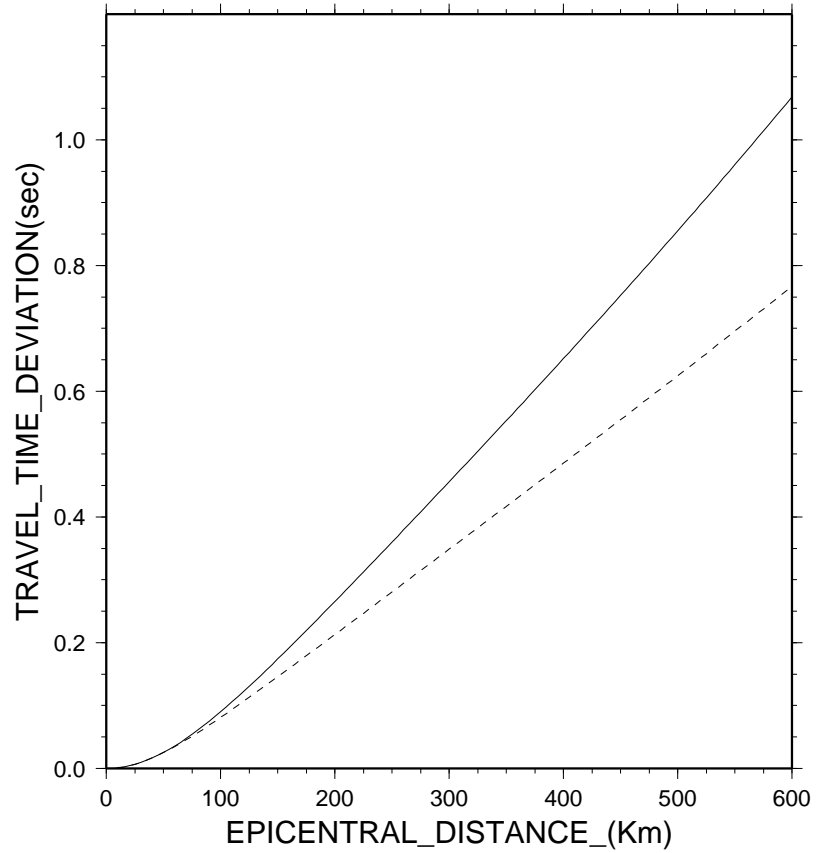
Figure 4.1: Travel time deviation $(t_{flat} - t_{sph})$ between flat and spherical earth models as a function of epicentral distance. The solid and dashed lines represent expected travel time deviations for hypocenters located at 150 and 100 km depth respectively.

4.3   Velocity Structure

The starting velocity structure for crust and upper mantle beneath central-eastern Peru was derived from surface wave studies over central Peru, Bolivia and northern Chile [James, 1971]. The original model was perturbed to take into account sedimentary layers of variable thickness as required for specific stations. Additionally V_p/V_s ratios were varied on the basis that crustal rocks present a Poisson's ratio of about 0.27 and mantle rocks present higher values known to increase with depth. Twelve intermediate focal depth earthquakes were used to examine the models with a selection criteria based on average root mean square residuals (RMS) and the Hypoellipse [Lahr, 1992] quality classification scheme.

The velocity model derived by this study, and henceforth called VMP85 (velocity model Peru 85), presented the best statistics for the twelve test events: an average RMS residual of 0.29, with 70% of the events rated as quality B, and 23% rated C. Table 4.2 shows the VMP85 model.

4.4   Station Corrections

Topographic effects on the network stations were modeled as an elevation correction that increases propagation times at a rate of 0.2 sec/km. The effect of sedimentary layers underlying the stations of CON, CGO, SEP and SJS, was introduced as a station delay. The correction factor representing the propagation delay under each of the stations was estimated as follows: P- and S-wave traveltimes were computed over a spherical model with a top layer representing the sedimentary cover; travel times were recalculated for these stations using VMP85. The time difference between the two models were introduced as station delays.

Table 4.1 summarizes the P- and S-wave propagation delays per event associated with stations CON, CGO, SEP and SJS, which were computed assuming a 2.5 km/s P-wave velocity in the sediments and a V_p/V_s ratio of 1.76.

4.5   Location Method

Travel time tables for P- and S-waves were generated for the VMP85 velocity model using the IASPEI91 [Kennett and Engdahl, 1991] procedure. These tables based on wave propagation through a spherically-symmetric earth model were used with Hypoellipse [Lahr, 1992] to determine the locations of the three intermediate focal events used in our study. Table 4.3 shows the hypocentral location and origin time for these events. The estimated uncertainties in distance and depth at the $\pm\sigma$ level were less than about 3 km. The origin time standard error was less than 0.37 seconds.

We can assess the stability of the hypocenters obtained using the VMP85 model by comparing them with the results obtained using the reference models of J-B [Jeffreys and Bullen, 1940] and IASP91 [Kennett and Engdahl, 1991]. Table 4.4 shows the results from the 3 models.

4.6   Travel Time Analysis to Coastal Stations

Travel time residuals are obtained by comparing travel times computed over a reference velocity model with the corresponding observed travel times. Table 4.5 shows the travel time residuals to coastal stations obtained with VMP85 velocity model. The table also shows a systematic pattern of negative residuals, which indicates that compressional wave propagation to these stations is faster than predicted. The residuals generally become more negative as epicentral distance increases although stations CHI and ETE, which are the northernmost, consistently exhibit larger residuals (about -4 sec).

The values of these residuals are too high to be attributed to phase mis-identification or inaccuracy in reference times, which have errors on the order of ±0.3 secs, and appears to be due to the influence of the high velocity slab. The results presented in Table 4.5 and the waveforms in figures $3.8 - 3.10$ demonstrate the complex nature of wave propagation within the region. To model the propagation of seismic rays through the 3-dimensional structure of the subduction zone we used a raytracing scheme described in the next chapter.

Table 4.1: Travel time corrections for stations located over sedimentary regions.

Station	Sediments (km)	Wave type	$delay_{101}$ (sec)	$delay_{181}$ (sec)	$delay_{270}$ (sec)
CGO	2.7	P	0.7	0.7	0.7
		S	1.3	1.2	1.3
CON	3.9	P	1.0	0.9	1.0
		S	1.9	1.7	1.8
SEP	4.2	P	1.0	1.1	1.1
		S	1.9	2.0	2.0
SJS	7.2	P	1.9	1.7	1.9
		S	3.4	3.0	3.1

Table 4.2: Velocity structure beneath central Peru-VMP85.

Depth (km)	V_p (km/s)	V_p/V_s
00.00	6.00	1.76
20.00	6.00	1.76
20.00	6.50	1.76
35.00	6.50	1.76
35.00	7.95	1.77
85.00	8.00	1.77
125.00	8.05	1.78
165.00	8.15	1.79

Table 4.3: Hypocentral locations for events E101, E270 and E181.

Event id	Date	Julian date	Origin time	Latitude (deg S)	Longitude (deg W)	Depth (km)	Rms
101	850601	152	04:35:55.0	10.95	73.97	110	0.25
181	850607	158	11:25:05.0	8.04	74.48	152	0.38
270	850614	165	06:21:42.6	9.24	75.94	121	0.29

Table 4.4: Comparison of hypocentral parameters as function of the velocity reference model.

Event	Model	Latitude (deg S)	Longitude (deg W)	Depth (km)	Rms
101	Iasp91	10.93	73.98	105	0.31
	J-B	10.89	73.97	103	0.42
	VMP85	10.96	73.98	109	0.25
181	Iasp91	8.05	74.49	148	0.40
	J-B	8.02	74.49	149	0.46
	VMP85	8.04	74.48	150	0.38
270	Iasp91	9.22	75.96	119	0.42
	J-B	9.20	75.95	118	0.51
	VMP85	9.24	75.94	121	0.29

Table 4.5: Travel time residuals at coastal stations associated with the 1-D velocity-depth model VMP85.

Event id	Station code	Δ (km)	Azm. (deg)	t_{obs} (sec)	t_{cal} (sec)	t_{res} (sec)
101	NNA	333	250	46.5	46.0	0.5
101	QUI	347	230	47.1	47.6	-0.5
101	GUA	389	210	51.5	52.7	-1.2
101	PAR	408	219	53.2	55.0	-1.8
181	NNA	508	210	67.6	67.7	-0.1
181	QUI	583	201	76.1	76.7	-0.6
181	ETE	606	281	75.2	79.4	-4.2
181	CHI	611	283	75.9	80.1	-4.2
181	PAR	672	197	86.1	87.3	-1.2
181	GUA	674	192	86.1	87.6	-1.5
270	NNA	319	197	43.6	44.7	-1.1
270	QUI	414	187	53.4	55.9	-2.5
270	ETE	498	300	62.1	66.1	-4.0
270	CHI	509	302	64.6	67.5	-2.9
270	PAR	510	184	65.0	67.5	-2.5
270	GUA	527	178	66.4	69.6	-3.2

Chapter 5

3-D RAYTRACING ANALYSIS

5.1 Introduction

Subduction zones are regions where oceanic lithosphere descends into the mantle. The cold subducting material generates large velocity variations which are common to these regions. The extent of these variations are expressed as velocity contrasts between the slab and the surrounding mantle ($\frac{V_{slab} - V_{mantle}}{V_{mantle}} * 100$). Several studies of subduction zones have reported velocity contrasts of $7 - 11\%$ for the Tonga-Kermadec region [e.g., Mitronovas *et al*, 1969; Mitronovas and Isacks, 1971; Bock, 1987], $2 - 15\%$ for the Japan region [e.g., Suyehiro and Sacks, 1979; Matsuzawa *et al.*, 1986; Iidaka *et al.*, 1991] and $6 - 11\%$ for the Central Aleutians [e.g., Engdahl and Gubbins, 1987].

In this section I present a model of slab structure of the subducting Nazca plate beneath northern-central Peru, based on constraints imposed by travel time residuals of P waves sampling in great extent the cold interior of the slab. Epicentral distances to recording stations ranged from about $3°$ to $6°$. The slab model, based on studies of seismicity and converted phases, includes three layers of different velocity: a top low velocity zone representing subducted oceanic crust, a thick and cold underlying peridotitic layer, and a transitional zone generated by the thermal contact between slab and underlying asthenosphere.

Propagation of P-waves through the slab is computed using raytracing techniques. Thicknesses and velocity contrasts within the uppermost two layers were varied to fit the observed data.

5.2 Slab Geometry

The upper boundary of the subducting Nazca plate used in this study is a slight modification of the slab model developed by Hasegawa and Sacks (1981). Figure 1.1 maps the isodepths contour to that boundary as dashed lines with labels on the trench and selected depths. In the study region, the oceanic slab subducts beneath northern-central Peru at an angle of 30° until it reaches an approximate depth of 100 km where it flattens and runs sub-horizontally for a distance of $300 - 400$ km to finally resubduct steeply into the upper mantle. The convergence rate in this region is about 100 mm/yr, and the trench follows a NW-SE orientation.

The major features supporting the model are summarized as follows:

- A Benioff zone geometry well constrained by studies of local seismicity and converted phases in central-southern Peru [Hasegawa and Sacks, 1981; Boyd *et al.*, 1984; Schneider and Sacks, 1987] and supplemented by the results of Schneider and Sacks (1991), Figure 3.1.

- Petrological and seismic studies revealing that the basaltic composition of oceanic crust in subduction zones can delay its basalt-ecoglite transformation under certain temperature and pressure conditions [Ahrens and Schubert, 1975; Fukao *et al.*, 1983; Sacks, 1983].

- Studies of anelasticity indicating values of Q= 1000 within the slab and Q= 500 within the crust and upper-mantle [Hasegawa and Sacks, 1981; Schneider and Sacks, 1991]. The high Q values (i.e., low seismic absorption of energy) apparently precludes the existence of asthenospheric material between the slab and the overlaying continental lithosphere.

- Heat flow studies reporting average values of $HF = 30 \ mW/m^2$ for the central Peru region which contrasts with higher values $HF = 60 \ mW/m^2$ observed over the adjacent southern volcanic province [Henry, 1981; Henry and Pollack, 1988]. The correlation

of the lower heat flow value with the continental geotherms developed by Chapman and Pollack (1977), suggest that a thick lithosphere, about 100 km, must underlain northern-central Peru. Similar to (c), this results supports the absence of asthenospheric material above the 100 km depth boundary.

5.3 Slab Structure

The slab model proposed in this study consists of a laterally-homogeneous 3-layer oceanic lithosphere:

- A thin oceanic basaltic crust with thickness of about 6 km [e.g. Fukao *et al.*, 1983, Matsuzawa *et al.*, 1986]. The rock composition in this layer are basalt and gabbros with density in the range of $2.8 - 2.9 \ gr/cm^3$ as inferred from laboratory analysis of ophiolite samples.

- An intermediate layer representing the subcrustal cold peridotitic lithosphere. [e.g. Ringwood, 1976; Anderson, 1987]. The lower boundary of this layer, as inferred from 3-D raytracing, appears to be located about 50 km beneath the upper slab-mantle interface.

- A transitional zone near the slab bottom, representing the contact thermal boundary between the slab and the underlying asthenosphere. Temperature gradients must affect this region whose composition is probably similar to the underlying asthenosphere. The extent of this zone is assumed to range between 10 and 15 km given that the age of the subducting plate constrains the total slab thickness to $60 - 70$ km [Sacks, 1983].

5.4 Raytracing Analysis

Method

Several numerical methods have been developed to study the wave propagation within laterally heterogeneous mediums using ray theory [e.g. Jacob, 1970; Julian 1970; Cerveny *et al.*, 1988; Vidale, 1990]. The method described here is based in part on Jacob's numerical approximation to the ray equations and follows the initial value approach (shooting method) as opposed to the boundary value approach (bending method) [Julian and Gubbins, 1977].

The data defining the upper boundary of the slab model are stored as longitude values corresponding to increments of 1 degree in latitude per 5 km depth. This is possible since the slab strikes approximately north-south. Intermediate points are obtained using a cubic-spline interpolation procedure with no overshoot [Wiggins, 1976]. The boundaries of the intermediate and bottom layers are obtained by extrapolating the upper boundary surface for fixed latitude and depth so as to preserve constant layer thicknesses. The step size of the raytracing, the velocity contrast and the thickness of the intermediate layer are input variables to the model.

The slab layers are modeled as laterally homogeneous structures and ray paths within them are computed stepwise at steps of 1 km. When a raypath encounters a slab boundary the seismic ray is projected onto that boundary and Snell's law is applied to calculate the azimuth and take-off angle of the outgoing ray.

An iterative process similar to the shooting method described by Julian and Gubbins (1977) is used to illuminate the coastal stations with a bidimensional fan of rays, which take off from a grid of angles and azimuths expanded about the pair (azimuth, take-off angle) obtained with the 1-D modeling. The grid of surface arrivals obtained in this way is compared with the station location, and the pair (azimuth,take-off angle) of the closest ray is taken as the center of a new grid. The process is repeated until a ray arrives within 250 m of the station.

We modeled different thicknesses for the layer representing the cold interior of the slab

(36, 40, 50 and 60 km) maintaining the uppermost (basaltic oceanic crust) constant in 6 km. A velocity contrast of -6% was selected for the oceanic crust [Fukao *et al.*, 1983; Matsuzawa *et al.*, 1986], while the contrast for the high velocity intermediate layer was varied over 5%, 7%, 8%, and 10% . Raytracing was done assuming that reflections can be generated at the bottom of the high velocity layer but we excluded propagation within the lower (transitional) layer.

Chapter 6

RESULTS

Raytracing through the subducting plate model gives the following results:

Event E101 : The seismic waves of this earthquake that propagate to coastal stations following a direct path, result in travel times at about the observed times for velocity contrasts of -6% and 8 in the basaltic (unconverted) crust and cold peridotitic interior respectively. Figures 6.1 to 6.4 show the propagation path of these rays in a cross section obtained projecting the slab and ray trajectory onto a great circle path between source and receiver. The residuals to stations GUA, PAR, QUI and NNA result in 0.1, -0.4, 0.0 and 1.3 sec respectively. The magnitude of these residuals are significantly smaller than those presented in Table 4.5 for the 1-D analysis. An exception is NNA whose travel time residual resulted in a larger value (1.3 with respect to 0.5 sec). I speculate this could have been caused by a lateral heterogeneity beneath the station given that first arrivals for the remaining two earthquakes present consistent residuals.

Event E270: As with event E101, seismic waves propagating along direct paths to coastal stations GUA, PAR, QUI, NNA, CHI and ETE presented travel times at about the observed values. Figures 6.5 to 6.9 show the corresponding cross sections for these results. However, no direct ray could be modeled for station PAR. The absence of direct arrivals to PAR is evident from Figure 6.10 which maps the 5 nearest arrivals to the station. It can be observed that when rays traveling to PAR arrive to the region where the slab boundaries change in slope, the seismic rays are defocused creating a shadow zone for direct rays to this station. Based on these results and assuming that reflections can occur at both boundaries of the cold interior layer, I investigated alternative propagation paths as shown in Figure 6.11. Based on these assumptions it was possible to find a ray with taking-off angle of $108.4°$

(clockwise from downward vertical) and with an azimuth of 5.1° that arrives at the station near the observed travel time. The travel time residual resulted in −0.85 sec compared with the −2.46 sec produced by the 1-D model.

Event E181: Event-station raypaths for this event, which is the deepest of the set (150 km) and is at the greatest epicentral distance from coastal stations, place a constraint on the thickness of the cold interior layer. Observations at stations ETE and CHI, which are the northernmost stations (Figure 1.1), are satisfied when first arrivals correspond to direct rays. For this to happen, a clear path must exist between the hypocenter and the corresponding stations. From Figure 6.12 and 6.13 we observe that this is possible only if the lower boundary of the intermediate layer is at least 50 km below the upper slab-mantle interface. Reflections were modeled but as expected resulted in propagation times longer than those observed. The residuals of about 4 sec observed at these stations with the 1-D velocity-depth model, were reduced to about 0.4 sec by our model. Raytracing for stations GUA, PAR, QUI and NNA resulted in no direct arrivals, a result due to a similar source-slab-station geometry to that found for station PAR and event E270. First arrivals to these stations are modeled as trapped waves within the intermediate layer, Figures 6.14 to 6.17.

The residuals obtained from the 3-D raytracing are summarized in Table 6.1 and have an average value of −0.1 sec in contrast with the −2.0 sec presented by the 1-D modeling. Thus, a slab structure with a 6 km basaltic crust underlain by a 44 km cold interior layer led to predicted arrival times consistent with the observations. Travel times marked with an asterisk in Table 6.1, correspond to propagation times associated with reflected rays. The last column (δ_{1D}) in the Table 6.1 corresponds to the 1-D travel time residuals.

Another result derived from 3-D raytracing is that the geometry of the slab, specifically the region where it changes significantly in slope, produces defocusing of the seismic wave-field. The regions not illuminated by seismic rays constitute shadow zones. In order to map the spatial distribution of seismic waves over the coastal region we generate a beam of rays leaving the sources of E101, E270 and E181 at equal steps of azimuth and take-off angles. The results are shown in Figures 6.18, 6.19, 6.20. Examination of these maps reveals the

strong relationship between shadow zones and slab geometry. It is also clear that there are no region of strong focusing caused by the slab geometry for these events.
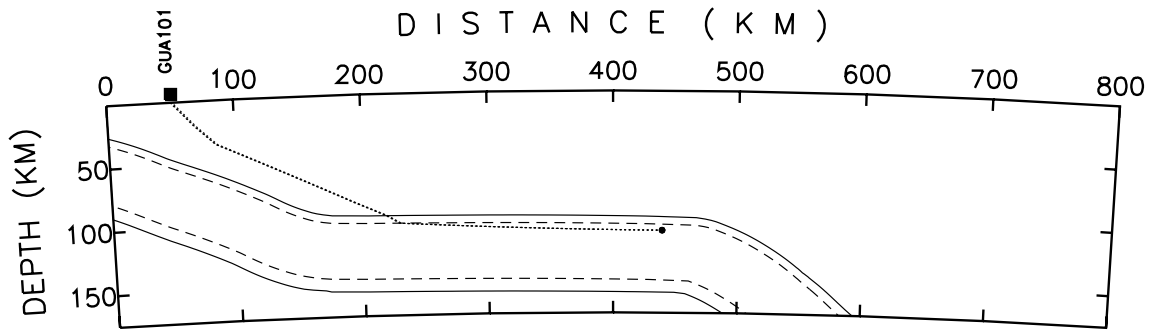
Figure 6.1: Direct arrival to station GUA, event E101

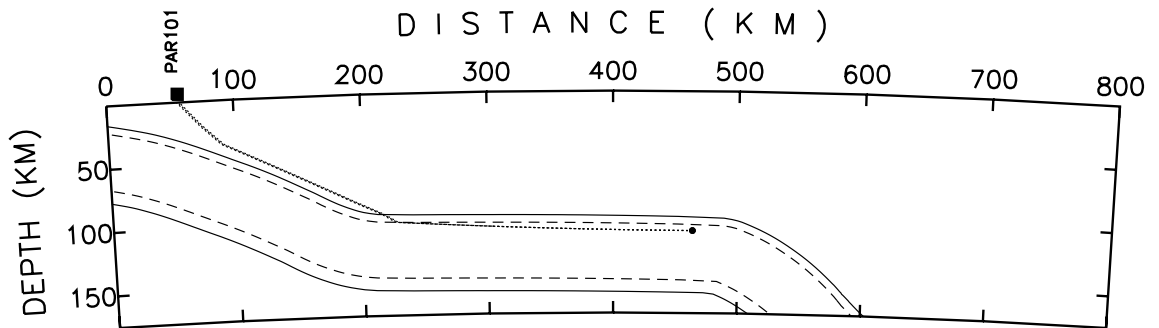Figure 6.2: Direct arrival to station PAR, event E101
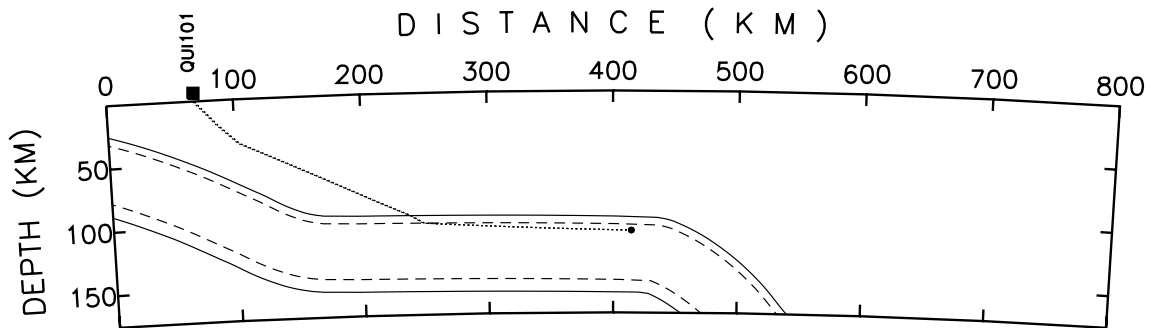
Figure 6.3: Direct arrival to station QUI, event E101

Figure 6.4: Direct arrival to station NNA, event E101
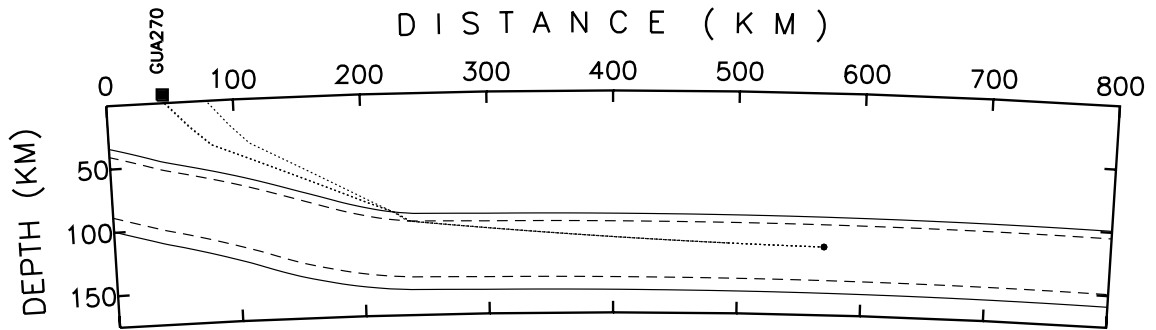
Figure 6.5: Direct arrival to station GUA, event E270.
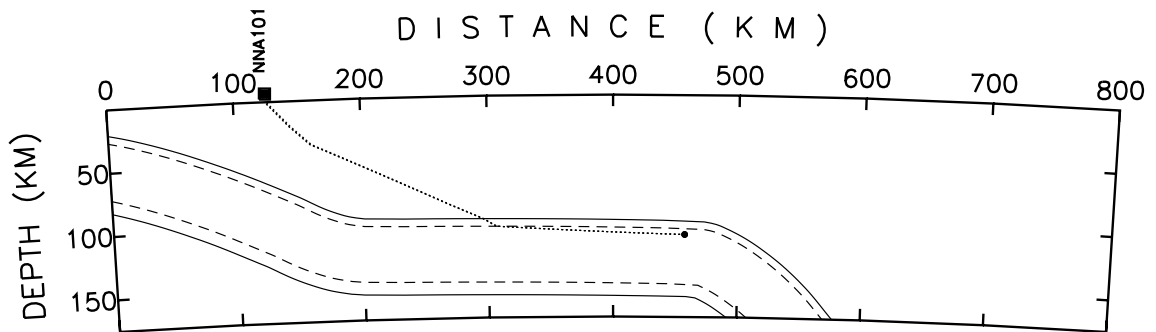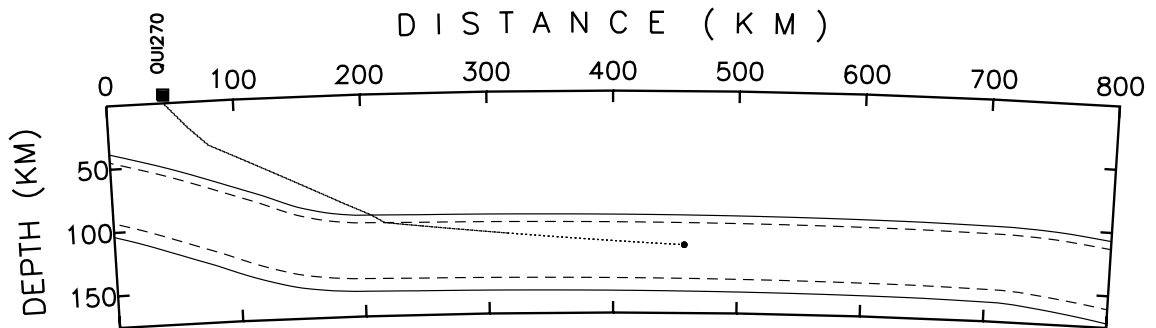
Figure 6.6: Direct arrival to station QUI, event E270.
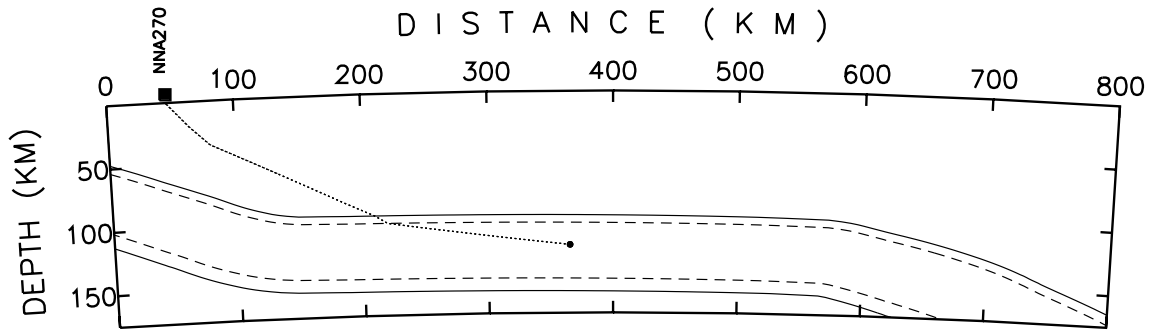
Figure 6.7: Direct arrival to station NNA, event E270.
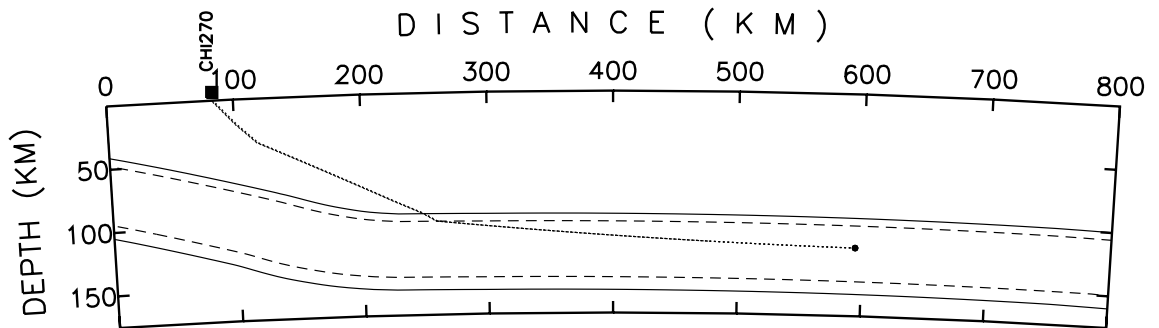
Figure 6.8: Direct arrival to station CHI, event E270.
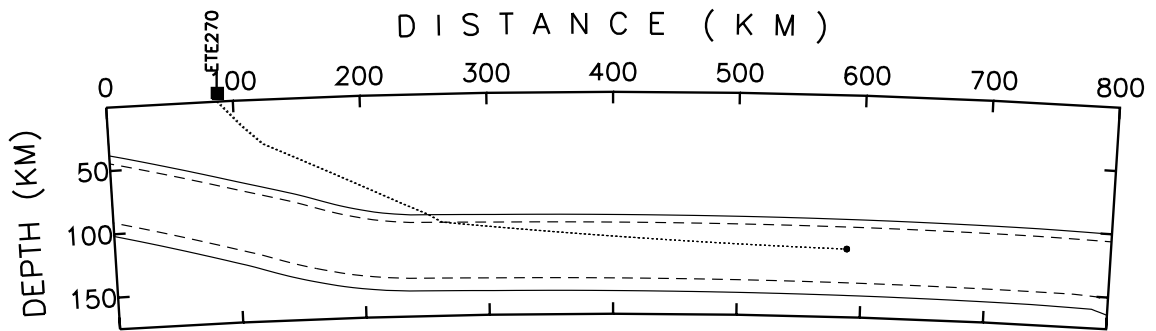
Figure 6.9: Direct arrival to station ETE, event E270.
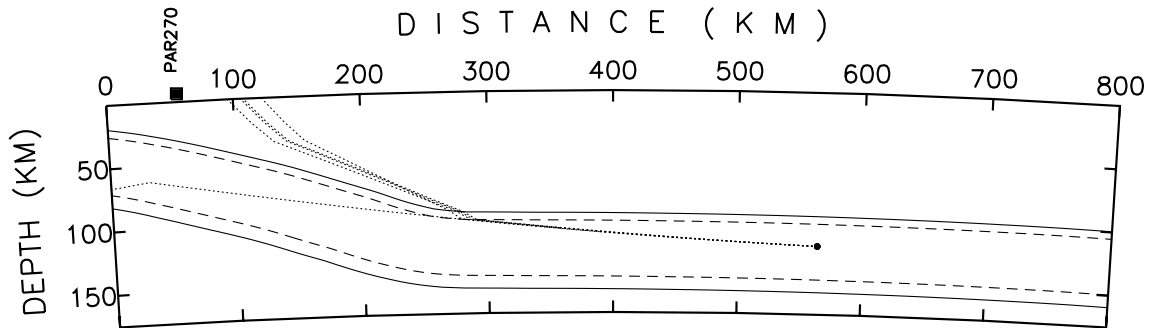
Figure 6.10: Direct arrival to station PAR, event E270. The change of slope in the slab causes the defocusing of direct rays.
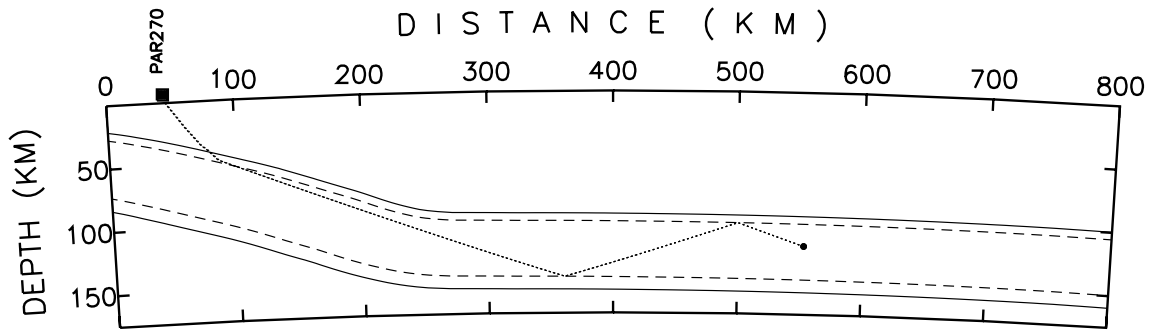
Figure 6.11: First arrival to station PAR, event E270.
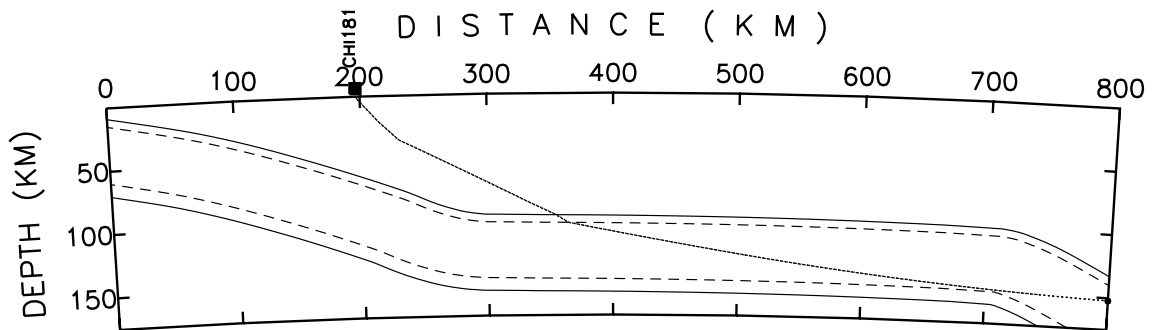
Figure 6.12: Direct arrival to station CHI, event E181.
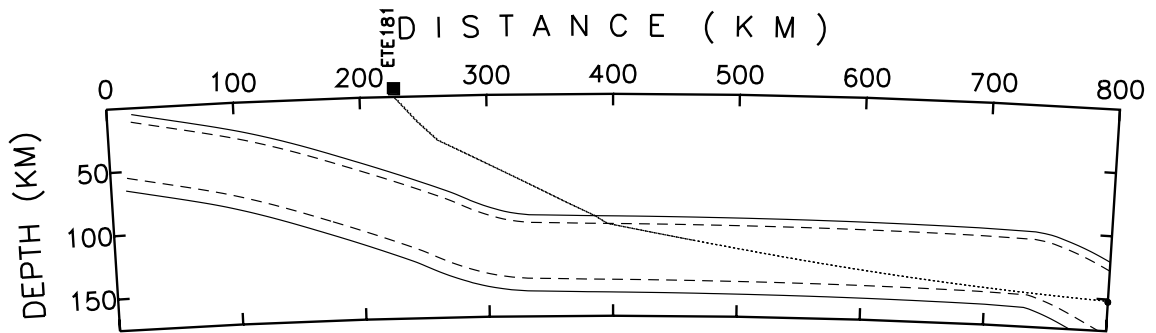
Figure 6.13: Direct arrival to station ETE, event E181.
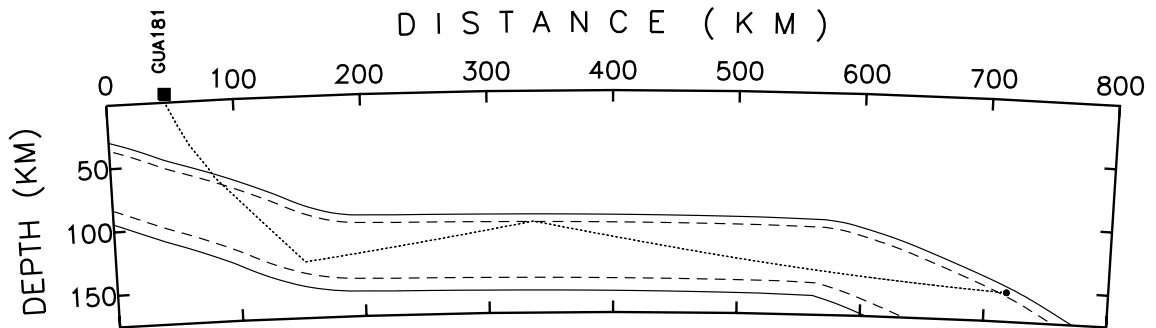
Figure 6.14: First arrival to station GUA, event E181 corresponds to a reflected ray bouncing at the bottom of the intermediate layer.
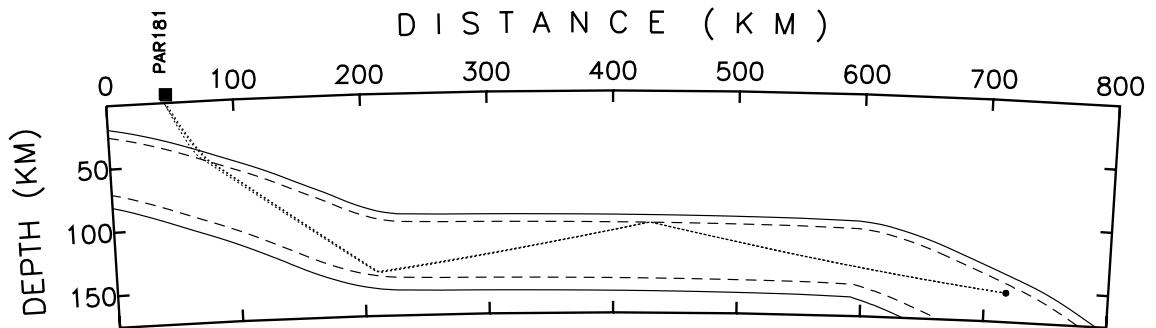
Figure 6.15: First arrival to station PAR, event E181 corresponds to a reflected ray.
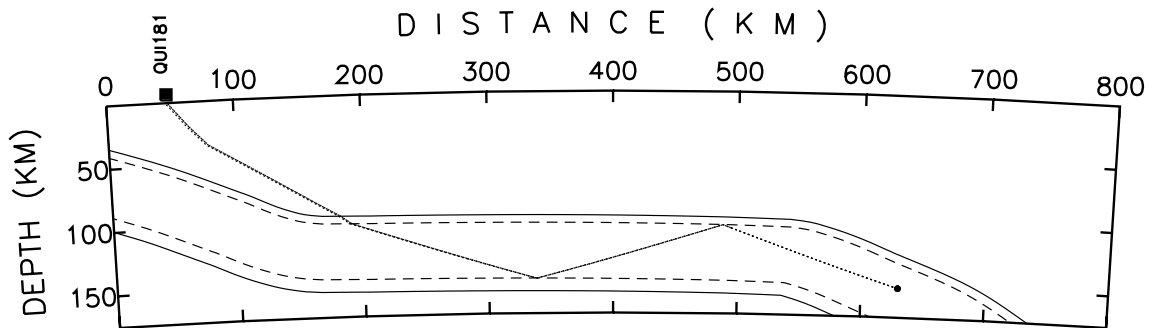
Figure 6.16: First arrival to station QUI, event E181, corresponds to a reflected ray.

Table 6.1: 3-D travel time residuals at coastal stations.

Event-id	TOBS (secs)	TCAL3D (secs)	δ_{3D} (secs)	δ_{1D} (secs)
GUA101	51.5	51.4	0.1	-1.2
GUA270	66.6	67.1	-0.5	-2.9
GUA181	86.6	*86.6	-0.1	-1.0
PAR101	53.2	53.6	-0.4	-1.8
PAR270	65.0	*65.8	-0.8	-2.5
PAR181	85.7	*85.3	0.5	-1.6
QUI101	46.8	46.7	0.1	-0.8
QUI270	53.7	54.4	-0.7	-2.2
QUI181	75.5	*75.8	-0.3	-1.2
NNA101	46.5	45.2	1.3	0.5
NNA270	43.6	43.9	-0.3	-1.1
NNA181	67.7	*67.8	0.1	-0.1
CHI270	64.6	63.9	0.6	-3.2
CHI181	76.0	76.0	-0.0	-4.1
ETE270	62.0	62.4	-0.4	-4.4
ETE181	75.3	75.5	-0.2	-4.2
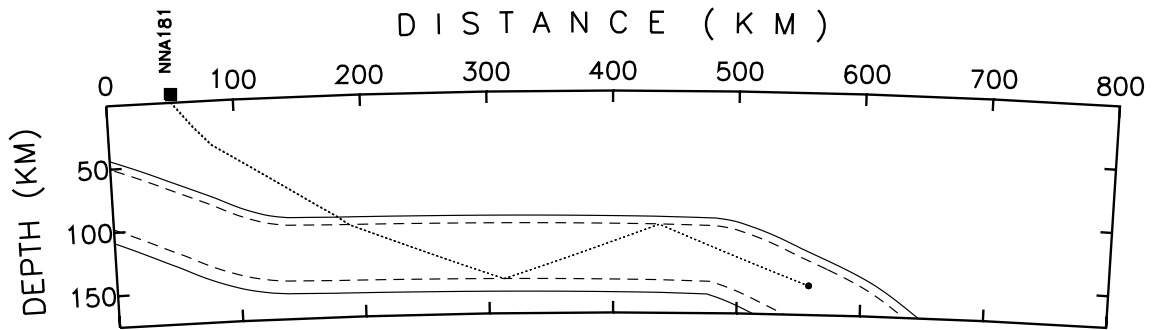
Figure 6.17: First arrival to station NNA, event E181, corresponds to a reflected ray.
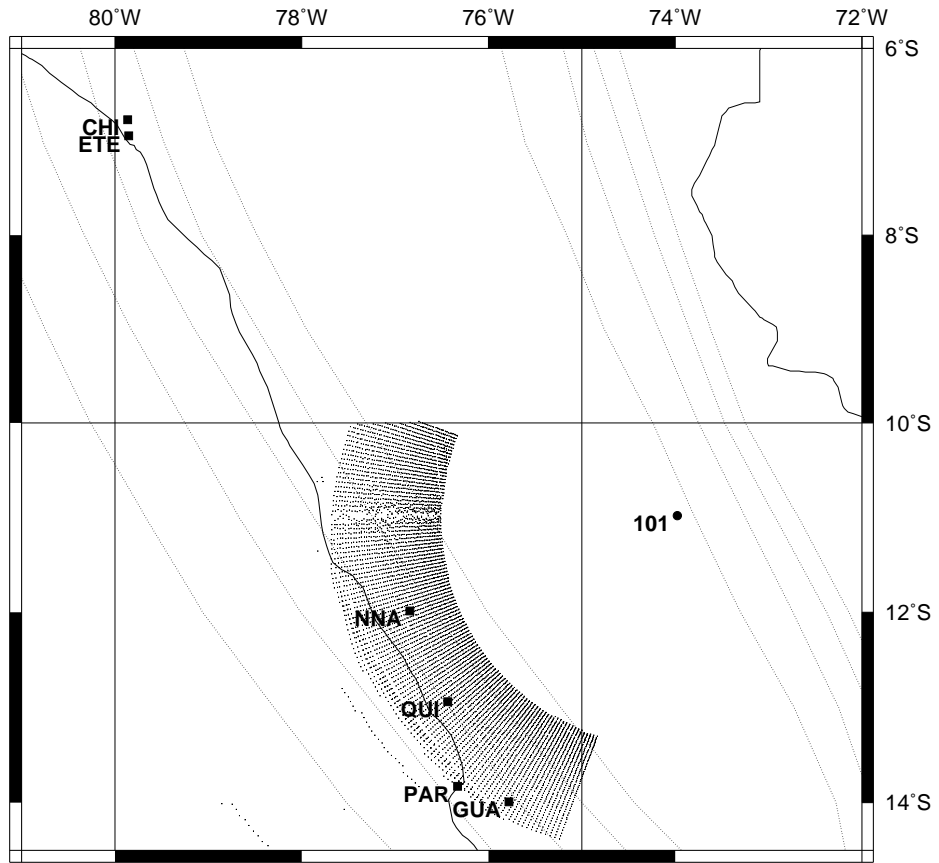
Figure 6.18: Mapping of surface arrivals for event E101. Gaps of arrivals delimit shadow zones generated by source-slab-station geometryy.
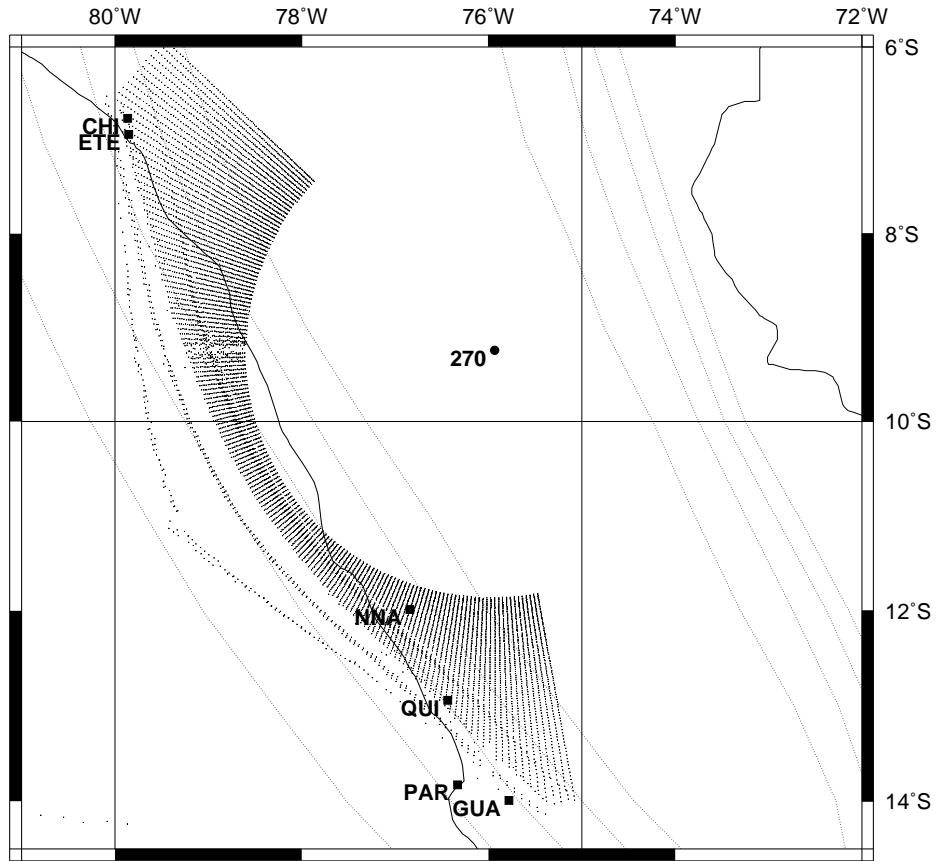
Figure 6.19: Mapping of surface arrivals for event E270. Station PAR270 is on the limit of a shadow zone.
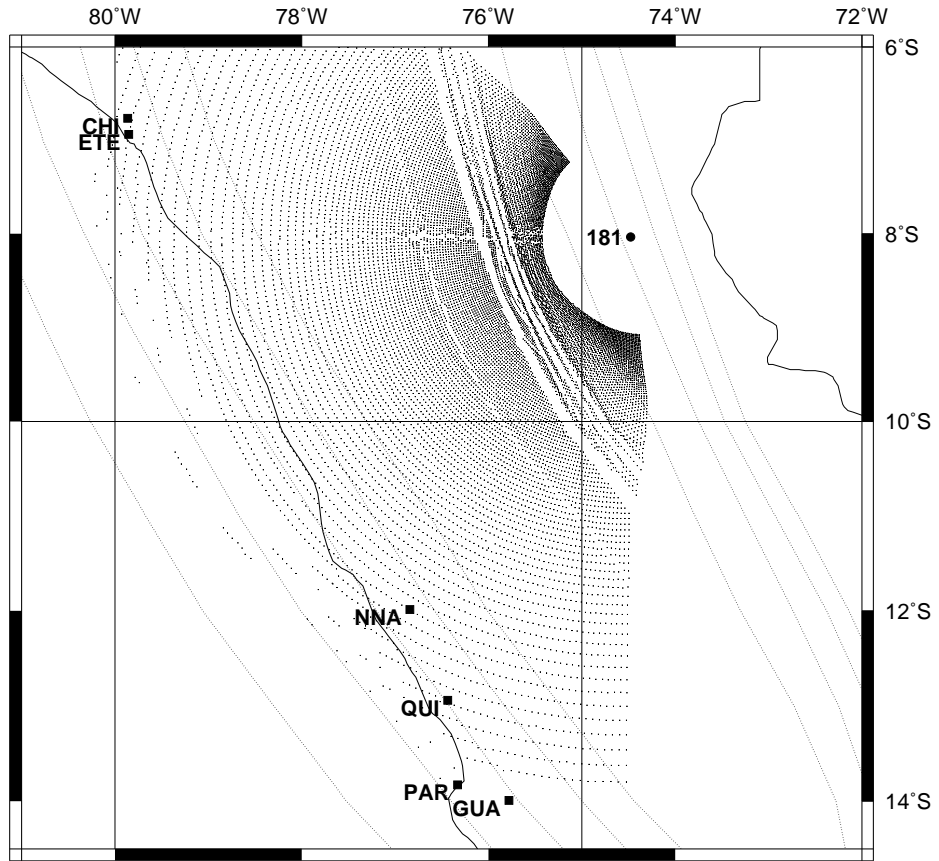
Figure 6.20: Mapping of surface arrivals for event E181. Stations GUA and PAR are within a shadow zone for direct arrivals.

Chapter 7
SUMMARY AND CONCLUSIONS

Travel time residuals observed at coastal stations in Peru for three accurately located intermediate-depth events in eastern Peru reveal a consistent pattern of early arrivals for a reference 1-D velocity depth model. Three-dimensional raytracing shows that the travel time residuals depend primarily on the reference velocity model, on the slab geometry, and on the propagation mode of seismic waves. We have used this information to place constraints on the structure of the Nazca plate subducting beneath central Peru.

Results for event E181 place a fundamental constraint on the the thickness of the cold intermediate layer. The hypocenter of E181, as can be observed in Figures 6.12 or 6.13, is located in the re-subduction zone. Seismic waves leaving the source can be expected to find a direct propagation path or be trapped in the intermediate layer before arriving at any coastal station. We found that when the thickness of the intermediate layer is less than 44 km, any direct propagation path will intersect the lower boundary causing the ray to refract into the lower regions. On the other hand, a trapped wave will eventually find a path to the station but with longer propagation times. It can be thought that a thinner layer and a trapped wave can result in a solution if higher velocities are assumed. Nevertheless this will result in a velocity contrast higher that the 8% proposed by this study which we regard as the upper limit of plausible values. Consequently, we constrain the lower boundary of the intermediate layer to be at a depth consistent with propagation of direct rays to stations ETE and CHI. The small residual times observed at the remaining coastal stations sustain our results.

Our preferred model was compared with similar models in which the velocity contrast in the intermediate layer was allowed to vary between 5% to 10%, but where the basaltic

layer kept a fixed velocity contrast of -6%. For velocity contrasts of 5% and 7% in the intermediate layer, the calculated travel times were greater than the observed values, while those computed assuming 10% resulted in earlier arrivals than observed. These results were the basis for the model presented in Figure 1.2 where the velocity structure within the basaltic layer is 6% less than the surrounding mantle and the velocity within the cold intermediate layer is 8% above the surrounding mantle.

The velocities proposed for the oceanic slab subducting beneath northern-central Peru are consistent with results reported in several other seismological studies in regions of normal subduction. However we should note that for the case reported here, the velocity contrast is required to occur at a shallower depth. This is a consequence of the different geometry existing between normal subduction zones [e.g. Tonga, Aleutians or Japan regions] and the horizontal subduction zone beneath northern-central Peru.

Recent studies of the slab-mantle interface [Helffrich, 1990; Helffrich *et al.*, 1992] find that differences in temperature and bulk composition in these regions constitute minor contributions to the observed velocity contrasts and propose that phase transformations in the mantle and slab mineralogies are the major contributing factors. Their model is based on reflection and conversions occurring at depths greater than 200, km where phase changes are expected (specially within the so-called transition region at depths greater than 400 km). In addition, it is known that laminated structures subject to shear stresses can acquire anisotropic properties [e.g. Babuska and Cara, 1991]. Because the subducting slab is subject to stresses in a direction normal to the trench, anisotropy may be expected to develop. The direction of fast polarization will be aligned with the stresses. Moreover, a recent study on mantle anisotropy reports observations of S-waves with the fastest polarization direction normal to the trench [Kaneshima and Silver, 1992]. The propagation paths studied here, however, are distributed over a broad range of directions relative to the trench. From this I conclude that anisotropy is not a contributing factor for the high velocities occurring within the subducting Nazca plate beneath northern-central Peru. It thus remain unknown what petrologic property produces the large velocity contrasts observed.

REFERENCES

[1] Gabbro-Ecoglite reaction rate and its geophysical significance. *Rev. Geophys. Space Phys. 13* (May 1975), 383–400.

[2] Thermally induced phase changes, lateral heterogeneity of the mantle, continental roots, and deep slab anomalies. *J. Geophys. Res. 92* (December 1987), 13968–13980.

[3] The earth as a planet: Paradigms and paradoxes. *Science 223* (January 1984).

[4] Mineralogy and composition of the upper mantle. *Geophys. Res. Lett. 11* (July 1984), 637–640.

[5] *Seismic Anisotropy in the Earth*. Kluwer Academic Publishers, Dordrecht, The Netherlands, 1991.

[6] Spatial distribution of earthquakes and subduction of the Nazca plate beneath South America. *Geology 4* (November 1976), 686–692.

[7] P-wave travel times from deep and intermediate depth earthquakes to local seismic stations and the subducted slab of oceanic lithosphere beneath the Tonga island arc. *J. Geophys. Res. 92* (December 1987), 13863–13877.

[8] High resolution determination of the Benioff zone geometry beneath southern Peru. *Bull. Seismol. Soc. Am. 74* (1984), 557–566.

[9] Complete seismic ray tracing in three-dimensional structures. In *Seismological Algorithms - Computational methods and computer programs*. Academic Press, 1988, ch. II.1, pp. 89–167.

[10] Regional geotherms and lithospheric thickness. *Geology 5* (May 1977), 265–268.

[11] Earthquake locations in island arcs. *Phys. Earth Planet. Inter. 30* (1982), 145–146.

[12] Relocation of local earthquakes by seismic raytracing. *J. Geophys. Res. 81* (1971), 4400–4406.

[13] A seismological constraint on the depth of basalt-ecoglite transition in a subducting oceanic crust. *Nature 303* (1983), 413–415.

[14] Observations of very high P-velocities in the subducted slab, New Zealand, and their relation with slab geometry. *Geophys. J. Int. 110* (1992), 238–250.

REFERENCES

[15]   Dispersion of P waves in subducted lithosphere evidence for an Ecoglite layer. *J. Geophys. Res. 96* (April 1991), 6321–6333.

[16]   Role of subandean fault system in tectonics of eastern Peru and Ecuador. *Memoir N2 of AAPG* (1963).

[17]   Subduction of the Nazca plate beneath Peru as determined from seismic observations. *J. Geophys. Res. 86* (June 1981), 4971–4980.

[18]   Study of the structure of the slab-mantle interface using reflected and converted seismic waves. *Submitted to J. Geophys. Int.* (July 1992).

[19]   *Study of the structure of the slab-mantle interface using reflected and converted waves.* Ph.d. diss., Department of Geology, Northwestern University, Evanston, Illinois, 1990.

[20]   *Terrestrial heat flow overlying the Andean subduction zone.* Ph.d. diss., University of Michigan, Ann Arbor, Michigan, 1981.

[21]   Terrestrial heatflow above the Andean subduction zone in Bolivia and Peru. *J. Geophys. Res. 93* (December 1988), 15153–15162.

[22]   FASTHYPO - A hypocenter location program. *Earthquake Notes 50* (1979), 25–37.

[23]   The P velocity within the Tonga Benioff zone determined from traced rays and observations. *J. Geophys. Res. 86* (May 1981), 3771–3782.

[24]   Three dimensional seismic ray tracing in a laterally heterogeneous spherical earth. *J. Geophys. Res. 75* (November 1970), 6675–6689.

[25]   Andean crustal and upper mantle structure. *J. Geophys. Res. 76* (May 1971), 3246–3271.

[26]   Structure and tectonics in the region of flat subduction beneath central Peru. part I: Crust and uppermost mantle. *Submitted Journal of Geophysical Research* (October 1992).

[27]   *Seismological Tables.* Brit. Assn. Gray-Milne Trust, 1940.

[28]   Andean tectonics related to geometry of subducted Nazca plate. *Geological Study of America Bulletin 94* (March 1983), 341–361.

[29]   Raytracing on arbitrarily heterogeneous medium. Tech. Rep. 1970-45, M.I.T. Lincol Laboratory, 1970.

[30]   Three dimensional seismic raytracing. *J. Geophys. 43* (1977), 95–114.

[31]   A search for source side mantle anisotropy. *Submited to J. Geophys. Res.* (December 1991).

REFERENCES

[32]   Travel times for global earthquake location and phase association. *Geophys. J. Int. 105* (1991), 429–465.

[33]   User's guide to HYPOINVERSE, a program for VAX and professional 350 computers to solve for earthquake locations. Open-File Report 85-515, U.S. Geological Survey, 1985.

[34]   HYPOELLIPSE/Version2.0: A computer program for determining local earthquakes hypocentral parameters, magnitudes and first motion pattern. Open-File Report 92-000, United States Department of the Interior Geological Survey, 1992.

[35]   HYPO71: A computer program for determining hypocenter, magnitude, and first motion pattern of local earthquakes. Open-file report, U.S. Geological Survey, 1972.

[36]   Estimation of thickness of a low-velocity layer at the surface of the descending oceanic plate beneath the northeastern Japan arc by using synthesized PS wave. *Geophys. J. R. Astron. Soc. 86* (1986), 767–787.

[37]   Model calculations of regional network locations for earthquakes in subduction zones. *Bull. Seismol. Soc. Am. 75* (April 1985), 397–413.

[38]   The Andean orogenic period and its major structures in central and northern Peru. *J. Geol. Soc. of London 141* (1984), 893–900.

[39]   Structure and evolution of the peruvian andes. In *The anatomy of mountain ranges.* Princeton University Press,N.J., 1987, ch. 10.

[40]   Seismic velocity anomalies in the upper mantle beneath the Tonga-Kermadec island arc. *J. Geophys. Res. 76* (October 1971), 7154–7180.

[41]   Episodic Cenozoic volcanism and tectonism in the Andes of Peru. *Earth Planet. Sci. Lett. 21* (1974), 213–220.

[42]   Spatial distribution of earthquakes and subduction of the Nazca plate beneath South America: a comment. *Geology 5* (September 1977), 576–577.

[43]   *Hypocenter locations and crustal structure inversion of seismic array travel times.* Ph.d. diss., University of Washingtoon, Seattle, Washington, 1973.

[44]   Plate reconstruction, aseismic ridges and low angle subduction beneath the Andes. *Geol. Soc. Am. Bull., Part I 92* (July 1981), 448–456.

[45]   Phase transformations in descending plates: implications for mantle dynamics and differentiation. *Geophysical Monograph, A. G. U.*, 19 (1976), 391–398.

[46]   Subduction of the young lithosphere. *J. Geophys. Res. 88* (April 1983), 3355–3366.

REFERENCES

[47] Stress in the contorted Nazca plate beneath southern Peru from local earthquakes. *J. Geophys. Res. 92* (December 1987), 13887–13902.

[48] Subduction of the Nazca plate beneath central Peru from local earthquakes. *unpublished* (1991).

[49] Subduction of the Nazca plate under Peru as evidenced by focal mechanism and by seismicity. *J. Geophys. Res. 80* (March 1975).

[50] Seismicity, fault plane solutions, depth of faulting and active tectonics of the andes of Peru, Ecuador and southern Colombia. *J. Geophys. Res. 88* (December 1983), 10403–10428.

[51] P- and S-wave velocity anomalies associated with the subducting lithosphere determined from travel-time residuals in the Japan region. *Bull. Seismol. Soc. Am. 69* (1979), 97–114.

[52] Analysis methods for kinematics data from local earthquakes. *Rev. Geophys. 24* (1986), 793–805.

[53] Finite-difference calculation of travel times in 3-d. *Geophysics 55* (1990), 521–526.

[54] Free software helps map and display data. *EOS, Trans. AGU 72*, 41 (October 1991), 445–446.

[55] A note on interpolating digitized curves. *Bull. Seismol. Soc. Am. 66*, 6 (December 1976), 2077–2081.

VITA

Edmundo O. Norabuena was born August 5, 1953 in Lima-Peru, the second and last son of Edmundo N. and Agripina Ortiz Norabuena. He attended middle and high school at a private school of the Maryknoll Catholic Congregation. After finishing, he enrolled at the National Engineering University in Lima-Peru, and graduated with a B.S. degree in Electronic Engineering in July, 1978. During his last semester as a senior he joined the Geophysical Institute of Peru as a research assistant in the Radio-astronomy division. While working, he enrolled in courses in System Engineering at the University of Lima for which in July 1982 he received a B.S degree. In 1983 he was assigned to install and maintain the Real Time Seismic Processing Center for the Peruvian seismic network. During that time he was member of the IEEE, computer society and of ACM (Association for Computing Machinery). In Spring 1991 he came to Virginia Polytechnic Institute and State University to pursue a Master degree in Geophysics. His areas of interest include software development for real time seismic applications, analysis of seismic wave propagation and seismic instrumentation.

Edmundo O. Norabuena after completion of his degree will rejoin the Geophysical Institute of Peru as a staff member.